Journal of Power Sources 556 (2023) 232518

Contents lists available at ScienceDirect

Journal of Power Sources

journal homepage: www.elsevier.com/locate/jpowsour

Longer cycle life and higher discharge voltage of a small molecular indanthrone resulting from the extended conjugated framework

Liyi Zhao [a], Yunfei Ning [a,b], Qingyu Dong [a], Zaka Ullah [c], Penghao Zhu [d], Surong Zheng [a,b], Guang Xia [a], Shoupu Zhu [e], Qi Li [a,b,*], Liwei Liu [a,b,**]

[a] Suzhou Institute of Nano-Tech and Nano-Bionics (SINANO), Chinese Academy of Sciences (CAS), Suzhou, Jiangsu, 215123, China
[b] School of Nano Technology and Nano Bionics, University of Science and Technology of China, Suzhou, Jiangsu, 215123, China
[c] Department of Physics, Division of Science and Technology, University of Education, Lahore, 54770, Pakistan
[d] Key Laboratory of Rubber-Plastics, Ministry of Education, Qingdao University of Science and Technology, Qingdao, Shandong, 261500, China
[e] College of Energy Storage Technology, Shandong University of Science and Technology, Qingdao, 266590, China

HIGHLIGHTS

- We proposed an extended molecular design to inhibit the dissolution of materials.
- The π-π stacking layers significantly enhanced the ionic and charge transport.
- A specific capacity of 238 mAh g^{-1} was achieved for IDT@IDT-1000 electrode.
- The extended conjugated framework endows the battery with longer cycle life.

GRAPHICAL ABSTRACT

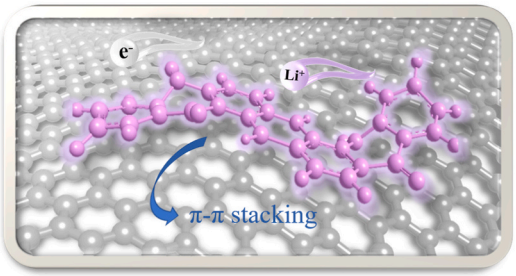

ARTICLE INFO

Keywords:
Structure design
Indanthrone
Intermolecular interactions
Organic cathode
Long cycle life

ABSTRACT

Organic cathodes have attracted wide attentions owing to their worthful advantages including higher capacity, abundant reserves and designable structure. However, significant dissolution of active organic materials hinders their practical applications in lithium-ion batteries (LIBs). Extending the conjugated framework in which intermolecular interactions play a crucial role, is an efficient strategy to inhibit the dissolution. Herein, an organic molecule with extended conjugated framework, indanthrone (IDT), is reported for LIBs. The rich carboxyl groups (C═O) ensure the high capacity for redox reactions, which is hence utilized as cathodic active centers. Moreover, the presence of C═O and amidogen resulted in plentiful intermolecular interactions, leading to insolubility and high stability. The rich functional groups also promote the chelation of oxygen and nitrogen with Li-ion and hence benefit their storage. A specific capacity of 238 mAh g^{-1} has been achieved for IDT-based cathodes at 0.2C, and a capacity of over 200 mAh g^{-1} is retained after 1000 cycles with a decay rate of only ~0.014% per-cycle. It is worth mentioning that there is a visible increase in voltage platform during cycling. The structure design of extending the conjugated framework endows the battery performance with longer cycle life and higher energy density.

* Corresponding author. Suzhou Institute of Nano-Tech and Nano-Bionics (SINANO), Chinese Academy of Sciences (CAS), Suzhou, Jiangsu, 215123, China.
** Corresponding author. Suzhou Institute of Nano-Tech and Nano-Bionics (SINANO), Chinese Academy of Sciences (CAS), Suzhou, Jiangsu, 215123, China.
E-mail addresses: qli2013@sinano.ac.cn (Q. Li), lwliu2007@sinano.ac.cn (L. Liu).

https://doi.org/10.1016/j.jpowsour.2022.232518
Received 11 July 2022; Received in revised form 19 November 2022; Accepted 9 December 2022

1. Introduction

Organic cathodes are auspicious choice for the fabrication of advanced green batteries owing to their worthful properties like flexibility, facile functionalization, high capacity, fast kinetics and assembly from renewable resources [1–3]. The mechanism of Li-ion insertion/extraction in organic cathodes is associated with reversible redox reaction of functional groups such as carboxylate, anhydride, keto, etc. [4,5]. In particular, quinone compounds with high electroactive carbonyl groups and devisable skeleton are anticipated to offer notable performance for organic Li-ion storage devices. However, till now, most of the carbonyl compounds offer poor performance in long-term cycling and rapid charge-discharge process [6,7]. Similar to Li–S cathodes, organic cathodes remained retarded for many years due to the dissolution of active molecules in electrolyte which leads to poor cycling stability. To tackle this issue, diverse strategies including polymerization of small molecules, immobilization of active species on conducting substrates, and salinization have been proposed and demonstrated [8–14]. Unfortunately, these strategies are not well adopted owing to their various disadvantages (e.g., polymerization and salinization reduce the ratio of active groups and hence lower the theoretical capacity of active materials, while loading inhibits dissolution partially due to the weak interactions). In this scenario, it is still essential to find new ways to resolve the dissolution problem for the development of high-performance rechargeable batteries.

The molecular design in organic semiconductors endows them with extended π-conjugated system which stabilizes the structure as well as facilitates the charge transport. Inspired from this approach, taking the advantage of extended molecular skeleton, we optimize the molecular design to improve the battery performance [15–20]. In other words, the inferior electrochemical behavior of small monomer molecules motivated us to focus on the structural study of well-defined redox-active molecules with extended conjugate skeleton. If the conjugate skeleton is properly expanded, the distribution of π-electrons cloud could be controlled and a stable planar structural system could be built. The extension of conjugate skeleton is also predictable to be highly conducive and to enhance the toleration for faster insertion/extraction of Li-ions during the fast charge-discharge process. Moreover, the conjugated system makes the charge distribution more uniform which is favorable to regulate the voltage platform [21–23]. Consequently, enlarging the conjugate frame has the opportunity to solve the dissolution problem, and meets the requirements of long cycling life for LIBs.

It is well known that the electron transport in extended conjugated molecules is limited due to intrinsic insulation of organic molecules which is critical to influence the electrochemical dynamics of batteries. Therefore, the active cathodes may have poor electron conductivity and low actual utilization rate. Interestingly, if the conjugated active molecules are combined with the conductive carbon layers to form a complete first order stack, it is possible to realize efficient transmission of electrons through strong π-π stacking effect. The π-π interaction is also advantageous to induce the stacking self-assembly process [24–28]. The conductive layers can be formed by carbonizing the conjugated molecules which may promote the affinity between raw molecules and carbonized layers [29]. Meanwhile, the π-π layers may produce voids containing lithium ions which are conductive to ion embedding/exiting during cycling. It is concluded that the stronger π-π interaction not only increases the stability of materials, but also considerably improves the electron transport and ion diffusion kinetics [30]. Therefore, the construction of π-π stacking layers is an efficient way to realize the higher actual capacity and faster rate of the battery.

Herein, we design a kind of carbonyl molecule, indanthrone (IDT), with extended conjugate skeleton, and construct the composites (IDT@IDT-1000) by stacking IDT with its carbonizing products to facilitate transport dynamics in batteries. Two soluble anthraquinones coupled with N-bridges form the large π-conjugated backbone. The multiple electroactive C═O units in IDT offer notable capacity for Li-storage, and its extended π-conjugated skeleton eases the charge transport in electrode. Furthermore, layers of IDT with carbide lamella serve as stable and high-rate host for Li-ions by enhancing π-π stacking and H-bonding interaction. In charge-discharge process, the IDT@IDT-1000 cathode delivered a specific capacity of 238 mAh g^{-1} at a current density of 0.2C with an average coulombic efficiency of ~99.0%, and offered a markable rate performance of 105 mAh g^{-1} at 5.0C. The current work introduces an effective approach to design the stable organic cathodes for lithium-ion batteries (LIBs) to accomplish the modern storage media demands.

2. Experimental section

2.1. Synthesis of IDT-1000

A certain amount of IDT (≥97%, Tokyo Chemical Industry, without any further purification) was annealed in CVD furnace. The temperature of the furnace was gradually increased to 1000 °C at a rate of 5 °C min^{-1}, and annealing of the sample was performed at this temperature in argon atmosphere for 4 h. Afterward, the temperature of the furnace was rapidly decreased to room temperature and the resultant product (named as IDT-1000) was collected. The final product was grinded and placed in a vacuum oven for later use.

2.2. Synthesis of IDT@IDT-1000

Equal amounts of IDT and IDT-1000 were dissolved in certain amount of deionized water, separately. Then, IDT-1000 solution was added to IDT solution dropwise under vigorous stirring. Afterward, the solution was sonicated several times to ensure the homogeneity. The resultant solution was poured into the Teflon-lined stainless-steel autoclave where it was heated at 180 °C for 24 h. Finally, the composite materials (IDT@IDT-1000) were obtained through centrifugation of the samples. The resultant samples were rinsed with deionized water and dried at 80 °C for 24 h.

2.3. Material characterizations

The morphology of IDT, IDT-1000 and IDT@IDT-1000 was observed using scanning electron microscopy (SEM, Quanta 400 FEG, FEI Co., Hillsboro, OR, USA, operating voltage = 20 kV) analysis. The elemental distribution of IDT@IDT-1000 was studied through energy-dispersive spectroscopy (EDS) mapping on SEM (Quanta 400 FEG, FEI Co., Hillsboro, OR, USA). The Brunauer-Emmet-Teller (BET) surface area and pore size distribution of IDT-1000 was recorded using a surface area and pore size analyzer (TriStar II 3020, Micromeritics Instrument Cope, USA). KBr pellets of the synthesized samples were prepared and their Fourier transform infrared (FTIR) spectroscopy analysis was carried out on a FTIR spectrophotometer (Spotlight 400/400 N, PerkinElmer, USA). The loaded amount of IDT was also determined through thermogravimetric analysis (TGA) (Q5000, TA Instruments, USA) in nitrogen atmosphere at temperature increasing rate of 5 °C min^{-1}. The X-ray diffraction (XRD) analysis was carried out on a X-ray diffractometer (XRD, D8 Advance with lynxEye and SolX; Bruker AXS, WI, USA; Cu-Kα radiation, λ = 1.5418 Å) for 2θ values from 10 to 90° at a scanning rate of 10° min^{-1}. X-ray photoelectron spectroscopy (XPS) results were received on a PHI instrument (PHI 5000 VersaProbe, Ulvac-Phi, Japan). The XPS spectra were treated for curve fitting using Shirley-type background subtraction approach.

2.4. Electrochemical measurements

The electrochemical performance of IDT@IDT-1000 cathode was analyzed by assembling the CR2025-type coin cells. The cathode slurry with 80 wt% IDT@IDT-1000, 10 wt% conductive carbon (Ketjenblack EC300J) as the conducting agent and 10 wt% polyvinylidene fluoride

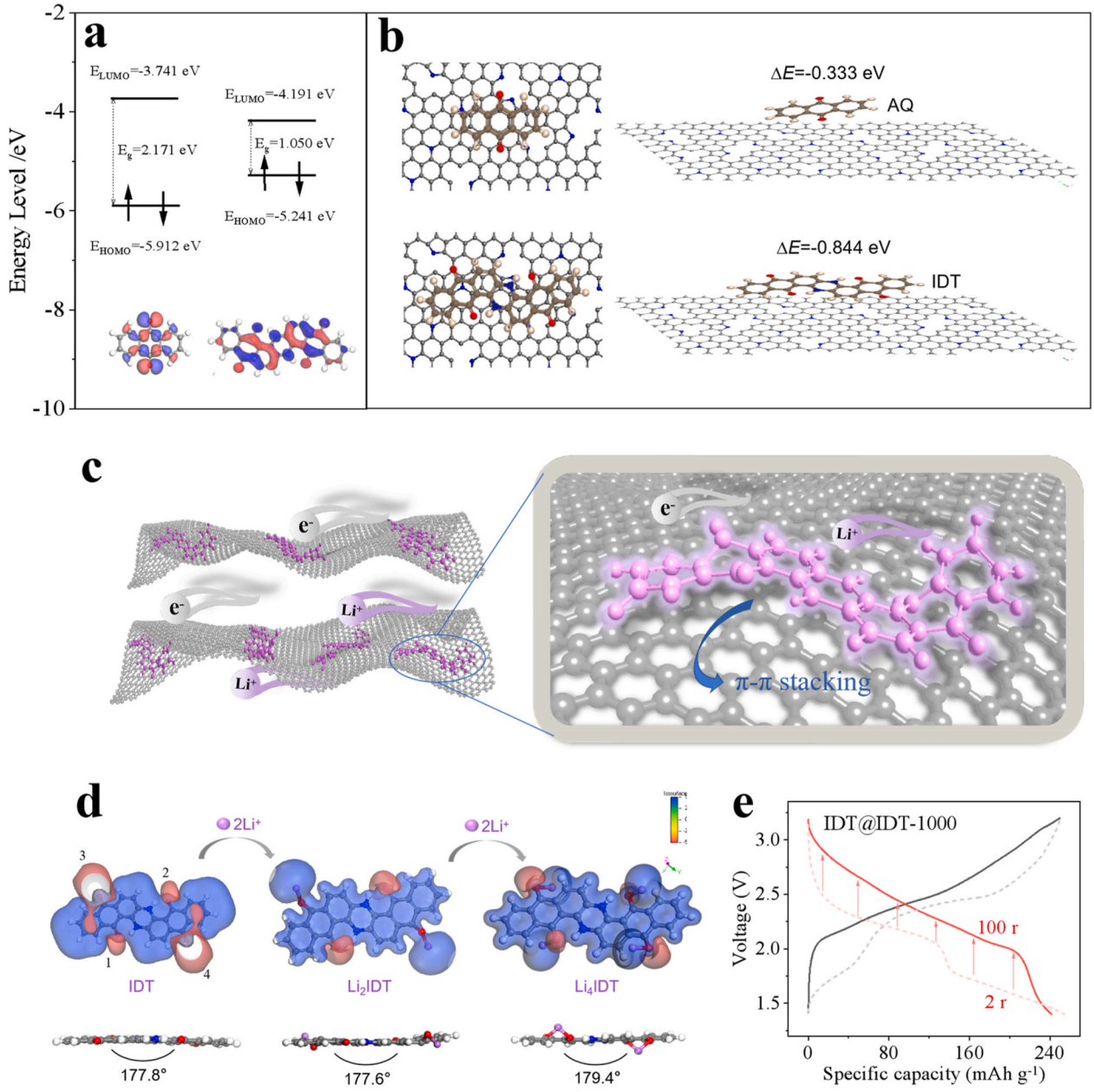

Fig. 1. (a) Chemical structure and calculated molecular orbital information of AQ and IDT. (b) Conformations and adsorption energy of AQ and IDT adsorbed by IDT-1000. (c) Schematic diagram of IDT@IDT-1000 showing the π-π interactions between IDT and IDT-1000. (d) Electrostatic potential distributions and geometry-optimized structure of IDT, Li_2IDT and Li_4IDT. (e) Galvanostatic charge-discharge profiles of IDT@IDT-1000 measured at 0.1C.

(PVDF) as a binder in solvent N-methyl-2-pyrrolidinone (NMP), were pasted on aluminum foil surface and dried in vacuum at 80 °C for 12 h. The slurry-coated aluminum foil was cut in the form of disks with a diameter of 1.3 cm and used as cathode. For electrochemical measurements, IDT@IDT-1000 cells were assembled in argon filled glove box. A lithium foil served as anode, a Celgard 2325 membrane worked as separator and LiTFSI in ethylene carbonate/diethyl carbonate (EC: DEC = 1:1 v/v) assisted as electrolyte in device fabrication. The cycling performance and rate capability of the fabricated cells were evaluated in voltage range 1.4–3.2 V at 25 °C on a battery test system (Shenzhen NEWARE, CT-3308-5V50Ma-s4, China). Whereas, the specific capacity was determined from mass of active materials. The cyclic voltammetry (CV) profiles were recorded on electrochemical workstation (CHI630D, Chenhua Instrument, China) for voltage between 1.4 and 3.2 V at the scanning rate of 0.1–1.0 mV s^{-1}. The electrochemical impedance spectrometry (EIS) was employed in frequency range from 1 MHz to 0.1 Hz. All the electrochemical measurements were executed at room temperature.

2.5. Computation methods

LUMO/HOMO calculations: DFT calculations were performed using the DMol3 module of Materials Studio software [31]. Geometric optimization and LUMO/HOMO energy calculations were performed using the generalized-gradient approximation Perdew-Burke-Ernzerhof (GGA/PBE) functional and double numeric polarization (DNP) basis set [32]. The convergence thresholds for energy, maximum force, and maximum displacement were set to 1.0×10^{-5} Ha, 2.0×10^{-3} Ha, and 5.0×10^{-3} Å, respectively.

Adsorption energy calculations: Adsorption energy calculations were performed using the Adsorption Locator module of Materials Studio software [33]. Force field Compass III and Surface region defined by

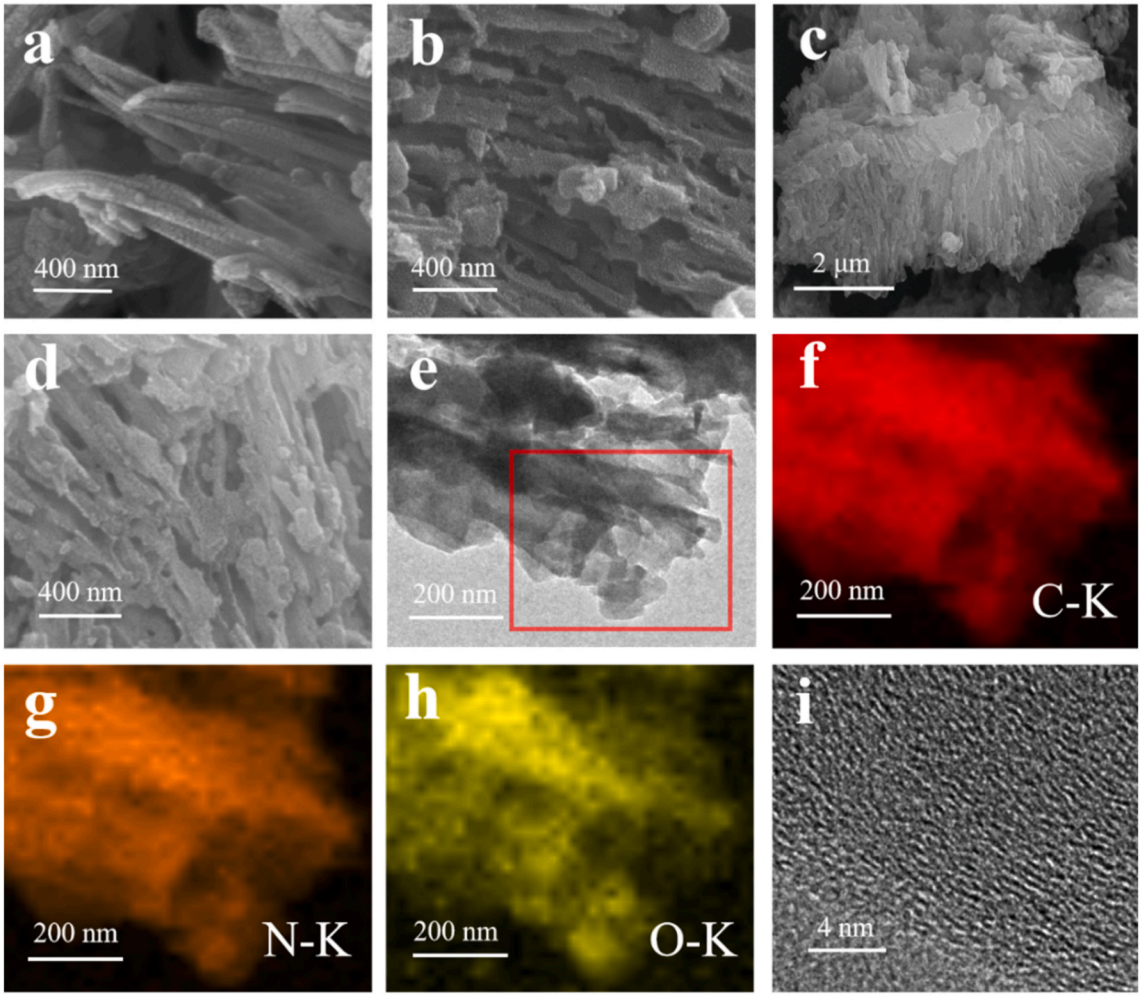

Fig. 2. SEM micrographs of (a) IDT, (b) IDT-1000 and (c, d) IDT@IDT-1000. (e) TEM micrograph of IDT@IDT-1000. EDS elemental mapping of (f) C, (g) N and (h) O for marked area in (e). (i) HRTEM image of IDT@IDT-1000.

field values set were applied for the simulation.

Band structure calculations: DFT calculations of IDT-1000 were performed using the CATSEP module of Materials Studio software [34]. Generalized gradient approximation (GGA) with PBE exchange correlation function was used for both geometry optimization and energy band structure calculations [35], and the plane wave cutoff energy was set to 400 eV. The space between the C1-xNx layers was set to at least 15 Å to eliminate the interactions between the layers. The geometry was optimized to relax until the force on each atom was less than 0.01 eV $Å^{-1}$ and the energy convergence criterion of 1×10^{-5} eV was satisfied. A $1 \times 1 \times 1$ k-point grid was used for the optimization of IDT-1000 [36].

3. Results and discussions

3.1. Construction and storage mechanisms of IDT@IDT-1000

Small molecular anthraquinone (AQ) materials have been widely investigated as cathodes owing to their two-electron reduction feature which furnishes these materials a notable theoretical energy density and makes them distinctive among common quinones. However, the high solubility of AQ and its discharged phase in electrolytes restrains its uses. Considering that an AQ dimer may show lower theoretical solubility on doubling the molecular weight, we creatively proposed to use commercially available indanthrone (IDT, also called Vat Blue 4) as active cathodes. The highest occupied molecular orbital (HOMO) and lowest unoccupied molecular orbital (LUMO) energy levels were calculated to investigate the effect of molecular structure on electronic structure of the materials [37]. As given in Fig. 1a, IDT showed the unoccupied molecular orbitals with energy levels of −4.191 eV, which were slightly lower than the lowest unoccupied orbital (−3.741 eV) of AQ. It suggests that IDT molecule is easier to get electrons and the onset reduction potential of IDT may be higher than that of AQ. Besides, the energy difference between HOMO and LUMO is called the energy band gap. It can be used as a measure of how easily a molecule can be excited. AQ and IDT showed the energy band gap of 2.171 and 1.050 eV, respectively. The narrower energy band gap of IDT suggests that the extended structure of conjugated systems is more easily excited, which is beneficial to the electrochemical reaction process of the cell.

However, due to the insulated nature of IDT, the storage performance of IDT was still low. To mitigate this issue, we designed a rational strategy to make IDT attached with carbonized conducted monolayers (Fig. 1c) for which the active materials were stabilized through π-π stacking interactions and H-bonding. Typically, carbonized IDT monolayers were prepared through direct carbonization of IDT at 1000 °C in Ar atmosphere. Fig. S1 shows the model structure and band structure for IDT-1000 from the calculation. The N content and type were determined from EDS and XPS tests and modeled as parameters for IDT-1000. The calculation results show that the bandgap of IDT-1000 was 0.317 eV. The nitrogen-doped carbon material (IDT-1000) opens the energy band gap and tunes the conductivity type. Its high free carrier density and active sites contribute to the improved conductivity and stability of the composite. After coating the IDT on the surface of IDT-1000, IDT@IDT-

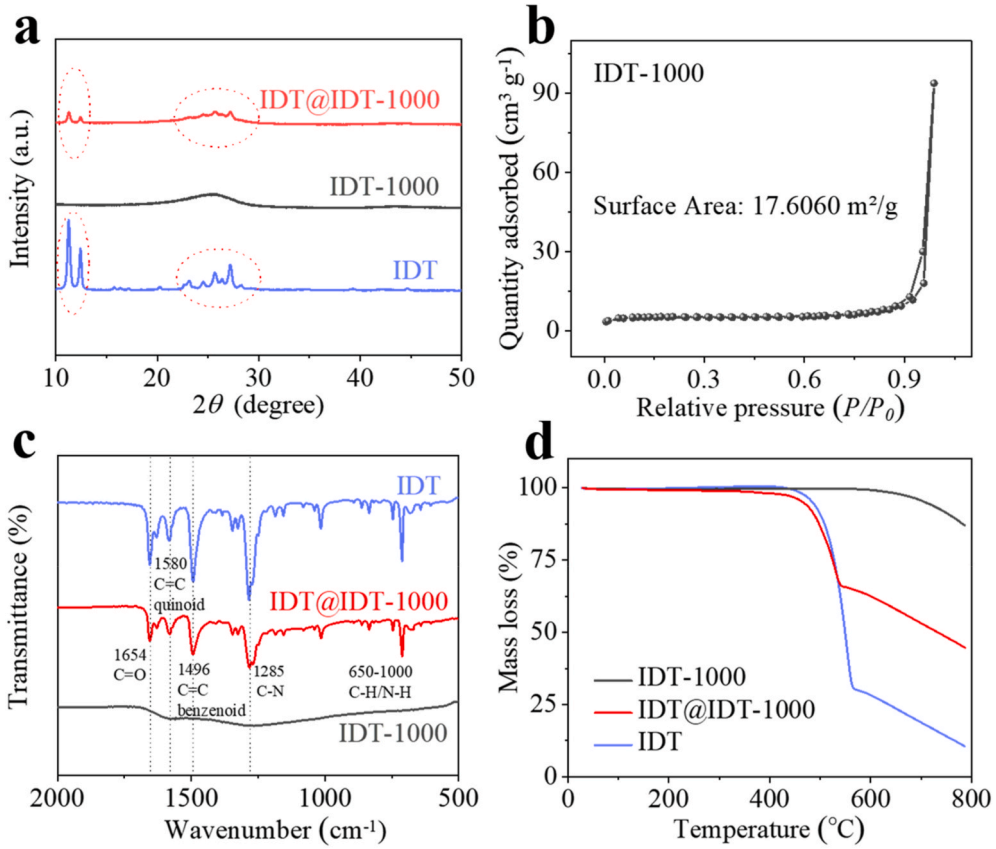

Fig. 3. (a) XRD patterns. (b) Nitrogen adsorption-desorption isotherms of IDT-1000. (c) FTIR spectra (KBr pellets). (d) TGA curves.

1000 with stable layered structure was obtained. Fig. 1b shows a comparison for the atomic conformations and adsorption energy of AQ and IDT adsorbed by IDT-1000. It is obvious that IDT is adsorbed on IDT-1000 with higher adsorption energy (−0.844 eV) than AQ (−0.333 eV). The higher adsorption energy evidences the development of strong chemical interaction between IDT and IDT-1000. The π-π interaction and H-bonding in IDT@IDT-1000 not only facilitated the stability of materials, but also considerably improved electron transport and ion diffusion kinetics.

To clarify the electrochemical stability, the electrostatic potential (ESP) distribution of IDT, Li_2IDT and Li_4IDT was calculated using DFT (Fig. 1d). IDT shows extremely negative ESP at ketonic oxygen regions which makes it more susceptible for electrophilic attacks of Li-ion. Moreover, it shows relatively even electron density distribution on framework which can effectually decrease the influence of cations and electron-deficient groups from electrolyte. The structural changes during the redox reaction process were also analyzed. The skeletons of IDT, Li_2IDT and Li_4IDT show nearly planar configuration with respectively angles 177.8, 177.6 and 179.4° which can efficiently encourage the charge delocalization and enhance the electrochemical stability.

To investigate the storage mechanisms of the prepared IDT@IDT-1000 cathode, half-cells were fabricated. As per a speculation, there were two voltage platforms due to the difference of C═O in position, like position 3, 4 and position 1, 2 as illustrated in Fig. S2. The position 1 and 2 are inclined to develop intramolecular hydrogen bonds (N–H···O═C) between the carbonyl group and amino group. However, during charge-discharge process, intra-molecular hydrogen bonds gradually became weaker and inter-molecular hydrogen bonds gradually became stronger due to π-π interactions between the layers. In this regard, π-π and hydrogen bond networks were formed and the positions of 1, 2, 3 and 4 were gradually homogenized. As given in Fig. 1e, two pairs of voltage platform at around 1.70 V, 2.25 V and 1.70 V, 2.46 V appeared which respectively correspond to decrease in conjugated carbonyl groups and reoxidation of alkoxide groups in first few cycles. Then the discharge voltage was increased as a whole due to the homogenization and dilution of electron cloud density on conjugated surface of the active material. The cyclic voltammetry (CV) test can further verify this conjecture. After 30 charge-discharge cycles, two divisive discharging platforms disappeared and a wider peak appeared in CV curve (Fig. S3). The relative wide peaks were attributed to multi-step redox processes. Moreover, the curves in consecutive three cycles showed significant overlapping, proving that IDT@IDT-1000 possessed great reversibility and higher structural stability during the electrochemical reactions.

3.2. *Materials characterization*

The surface morphology and microstructure of IDT, IDT-1000 and IDT@IDT-1000 were investigated through scanning electron microscopy (SEM) and transmission electron microscopy (TEM) analyses. Fig. 2a depicts the fibrous structure of IDT materials. After pyrolysis, IDT-1000 shows some layered structure (Fig. 2b) which is different from that of IDT. Fig. S4 shows energy-dispersive X-ray spectroscopy (EDS) results for designated region of IDT-1000 which evidence that the elemental composition of IDT-1000 (C, N and O) remains same after the pyrolysis. Owing to robust π-π interactions and H-bonding, morphology of IDT-1000 seems to be stacked in similar fashion to that of graphene sheets. Fig. S5 shows the HRTEM image of IDT-1000. Generally, the presence of disorder can alter the d-spacing of material. The d-spacing for IDT-1000 is found to be 0.38 nm. The value is slightly higher as compared to the ordered graphitic carbons (0.34 nm). It provides more sites for efficient Li-ion transport. The morphology of IDT@IDT-1000 at different resolutions is shown in Fig. 2c, d, i. It is similar to that of layered IDT-1000, suggesting that the IDT-1000 structure is well

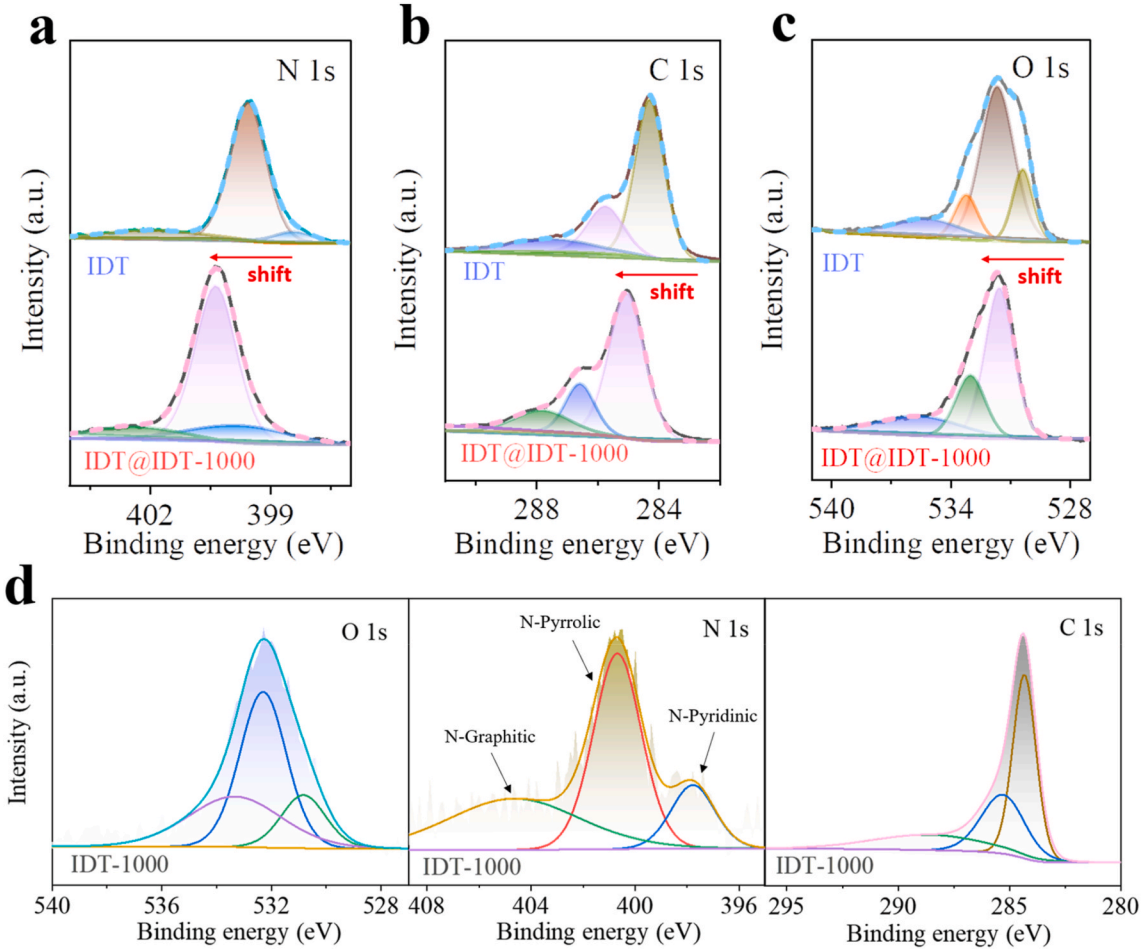

Fig. 4. High-resolution XPS spectra of (a) N 1s of IDT and IDT@IDT-1000, (b) C 1s of IDT and IDT@IDT-1000, (c) O 1s of IDT and IDT@IDT-1000, and (d) C 1s, N 1s and O 1s of IDT-1000.

sustained without structural damages after attaching with IDT. The uniform layered structure of IDT@IDT-1000 also shows a very homogeneous distribution of IDT in IDT-1000. The uniform elemental mappings of C, N and O given in Fig. 2e–h, support this suggestion. It is further revealed that the IDT particles can be attached onto the surface of IDT-1000 layers and can increase the structure stability significantly.

X-ray diffraction (XRD) analysis was conducted to examine the crystal structure of IDT in IDT@IDT-1000. As shown in Fig. 3a, the diffraction peaks of IDT and IDT@IDT-1000 arose at 2θ value ~11.2 and ~27.2° which suggest that the crystal structure of IDT in IDT@IDT-1000 was not destroyed. The enlarged XRD pattern of IDT-1000 (Fig. S6) shows the intense and broad diffractions at 2θ values 25.2 and 43.8° which respectively correspond to planes (002) and (101) for graphite. Such broad and intense peaks may be due to formation of disordered graphitic phase. Moreover, the (002) peak is shifted towards lower value of 2θ relative to its value for pure graphite (26.5°) which indicates the increase in d-spacing. The broadening of peaks confirms the increase in disorders in IDT-1000 which is highly desired for Li-ion storage. Presence of nano-cavities in IDT-1000 was also investigated through BET surface area analysis. Fig. 3b displays the corresponding adsorption-desorption isotherms for IDT-1000. The specific surface area of IDT-1000 was calculated as 17.606 $m^2\ g^{-1}$. Besides, there were rich mesopores and macropores of IDT-1000 (Fig. S7), which was due to the presence of gaps between ultrathin nanosheets. Such a porous structure with distributed hierarchies could be suitable for efficient ion/electron transport applicability. These results are consistent with previous outcomes for Li-ion storage.

In order to further examine the structures of IDT@IDT-1000, FTIR spectroscopy was carried out (Fig. 3c). The absorption peak in FTIR spectrum of IDT arose at ~1654 cm^{-1} which can be attributed to C═O bond. The peaks around 650-1000 cm^{-1} are ascribed to C–H and N–H vibrations. As compared to IDT spectrum, IDT@IDT-1000 spectrum shows the similar but suppressed C═C peaks for quinoid and benzenoid units at respectively 1580 cm^{-1} and 1496 cm^{-1} which can be due to π-π interactions and H-bonding among them. The results also evidence the transfer of charge between IDT and IDT-1000.

The thermal behavior and composition ratio of IDT@IDT-1000 were investigated through TGA. The sample was heat-treated at increasing temperature rate of 10 °C min^{-1} in N_2 atmosphere and its weight loss was recorded. The curves in Fig. 3d reveal that the IDT, IDT-1000 and IDT@IDT-1000 have relatively good thermal stability up to 400 °C. After that, IDT and IDT@IDT-1000 started to degrade rapidly at ~500 °C. The weight of IDT attached to IDT-1000 was ~50% as was measured during this analysis.

To evaluate the π-π interactions in IDT@IDT-1000, XPS analysis was conducted. High-resolution XPS spectra (Fig. 4a–c) show that N1s peak of IDT has good symmetry with a distinct characteristic peak at 399.6 eV. Compared to IDT, N1s peak of IDT@IDT-1000 undergoes significant splitting and shifting, with the feature peaks appearing at 399.8 eV, 400.5 eV and 402.4 eV which can be credited to the π-π interaction between IDT molecules and IDT-1000 scaffolds. Meanwhile, the peak positions of C1s and O1s were also shifted. The shifting of peak position is associated with the density of electrons in outer layers of the element. The decrease in electron density increases the ability of corresponding element to bind the electrons outside the nucleus. The results validate the successful assembly of IDT@IDT-1000 through layer-by-layer

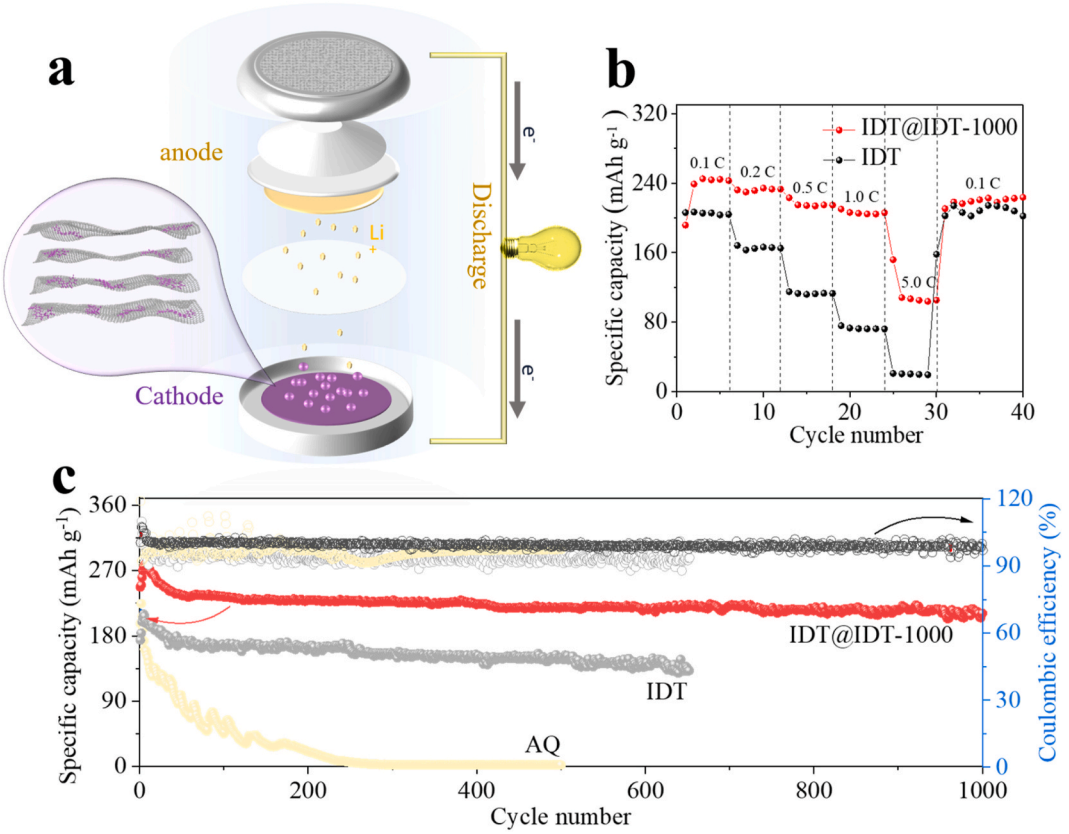

Fig. 5. (a) Schematic illustration showing the configuration of battery. (b) Rate performance of IDT and IDT@IDT-1000 measured at the current density of 0.1–5.0C. (c) Cycling performance of AQ, IDT, and IDT@IDT-1000 cathodes recorded at a rate of 0.2C.

stacking. The π-π interactions between the layers dilute the electron density and increases the binding energy of C and N, resulting in peak shift phenomenon. Fig. S8 shows the XPS spectra of IDT, IDT-1000 and IDT@IDT-1000. The existence of graphitic structural phase in IDT-1000 is also evidenced. Fig. 4d shows C1s XPS spectrum of IDT-1000 in which a sole narrow peak at 284.4 eV clearly shows the presence of graphitic carbon.

3.3. Electrochemical performance of IDT@IDT-1000

In order to investigate the electrochemical performance of IDT@IDT-1000 and verify its potential application in LIBs, AQ, IDT and IDT@IDT-1000 were assembled in half cells with Li as counter electrode (Fig. 5a). The electronic conductivity of AQ, IDT and IDT@IDT-1000 electrode coatings (Table S2.) were 1.96×10^{-4}, 4.00×10^{-4} and 1.01×10^{-2} S/cm, respectively. The higher electronic conductivity of IDT@IDT-1000 cathode can facilitate fast reaction kinetics and increase actual discharge capacity. The electrochemical tests in Fig. S9 indicated that the onset reduction potential of IDT was higher than that of AQ, which was consistent with the analysis of lowest unoccupied molecular orbital (LUMO) energy levels. A higher capacity of 105 mAh g^{-1} was recorded even at a fast rate of 5.0C for IDT@IDT-1000 electrode (Fig. 5b). After decreasing the rate to 0.1C, the capacity was improved to >200 mAh g^{-1} and remained stable at this value for the following cycles. The selected charge-discharge profiles at varying current density are given in Fig. S10. Based on this encouraging result, we further tested its long-term cycling performance for 1000 cycles at a rate of 0.2C (Fig. 5c). The IDT@IDT-1000 electrode showed a stable capacity of >200 mAh g^{-1} and an average coulombic efficiency of more than 99.0% after 50 cycles. The high discharge capacity suggests the complete Li-ion insertion in redox active sites. The instability of the first few cycles may be due to material activation, and the reconstruction of π-π interactions and H-bonding. Fig. S11 shows the charge-discharge voltage profiles of different cycles which were associated with the variation characteristics of long-term cycling. More detailedly, Fig. S12 certifies that the IDT@IDT-1000 electrode preserves the original structure and did not receive any damages during the repetitive charge-discharge cycles. Fig. S13 shows that the IDT@IDT-1000 electrode possesses an excellence capacity retention in a long cycle compared with several other extended materials including BAQB, Br_3TOT, BBQB, PT, SSDC, and oIDT. It greatly illustrates the superiority of the extended conjugate molecule strategy.

The fast reaction kinetics of IDT@IDT-1000 were evaluated by measuring the CV profiles at various scan rates from 0.1 to 1.0 mV s^{-1}. Fig. 6a shows the anodic and cathodic peaks recorded at different scan rates. It is obvious from CV curves that the peak current gradually increases as the sweep rate increases exponentially, with oxidation and reduction peak shift respectively to higher potential and lower potential. The peak current i and sweep rate v are recorded for the different scan rates which makes it is possible to determine that whether the redox reaction is controlled by surface or by ion diffusion. The voltammetric response of the ideal electrode at different sweep rates are calculated using the following equation:

$$i = av^b$$

where, i denotes test current, v indicates sweep rate, and a and b are variable parameters. When the value of slope b is approaching to 1, the system is mainly driven by capacitive storage mode. When the value of slope b is near to 0.5, the system is mainly controlled by ion diffusion mode. The adjustable parameter b for IDT@IDT-1000 was 0.66 (Fig. 6b) which indicates that the capacity of the cathode is controlled by both the capacitive storage mode and ion diffusion mode. The graphene-like layered structure of IDT-1000 has a large number of N-doping sites and a continuous ion electron transport path; thus has a certain surface

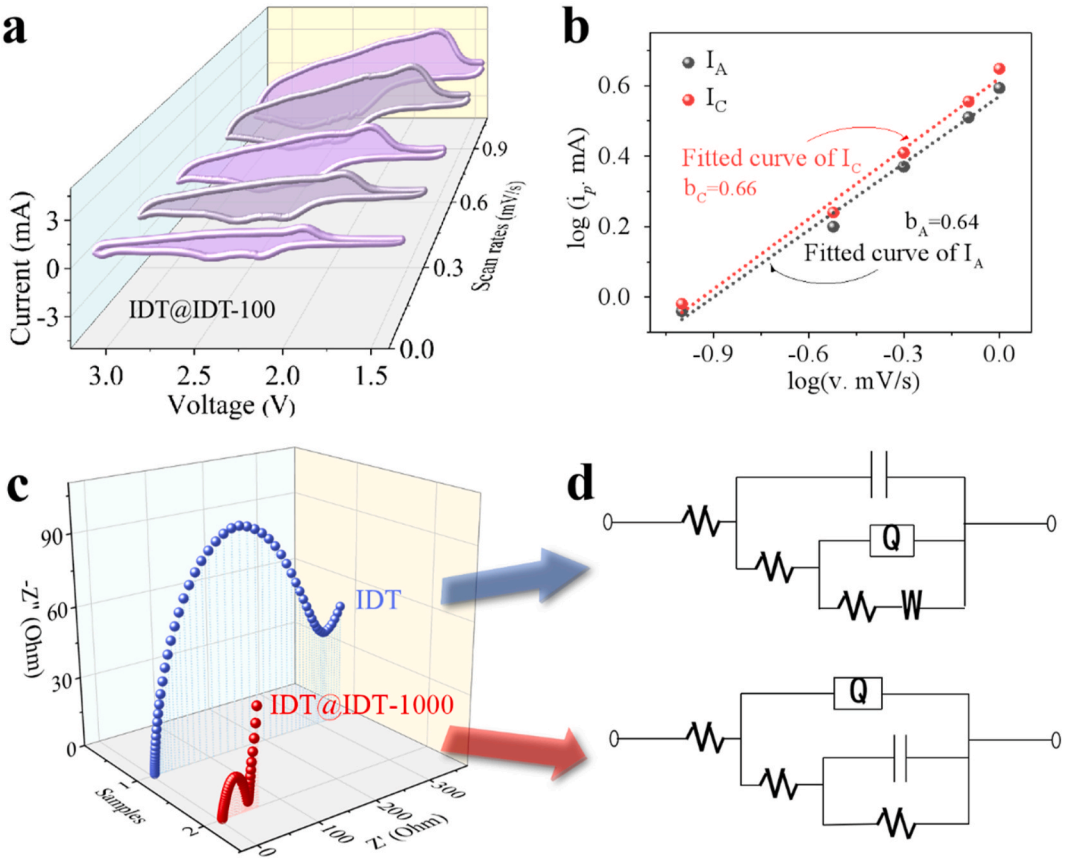

Fig. 6. (a) CV profiles of IDT@IDT-1000 electrode recorded at varying scan rates. (b) Respective log *ip* vs log *v* of IDT@IDT-1000 electrode. (c) Nyquist plots for IDT and IDT@IDT-1000 electrodes. (d) Equivalent circuit model of IDT and IDT@IDT-1000 electrodes.

capacitive contribution which also indicates the fast response kinetics of the IDT@IDT-1000 cathode material.

EIS analysis was performed in frequency range of 1 MHz to 0.1 Hz to further investigate the kinetics of electrochemical reactions in IDT@IDT-1000 electrode (Fig. 6c). High frequency region of Nyquist plots shows a semicircle, whereas their low frequency region gives an inclined line. The small semicircle evidences the improved kinetics of Li-ions migration through SEI film and rapid charge transfer reaction. The inclined line with large phase angle suggests lower Warburg impedance which signifies the diffusion of Li-ions in IDT@IDT-1000 electrode. Faster ion diffusion efficiency and lower charge transfer impedance influence the reaction kinetic characteristics. The EIS spectra obtained from the tests were fitted to the equivalent circuit; Fig. 6d shows the fitted equivalent circuit models. The measured and calculated Nyquist plots of IDT and IDT@IDT-1000 electrodes are shown in Fig. S14, where Table S1 gives the details of fitted EIS data corresponding to the two electrodes. The results show that the IDT@IDT-1000 cathode has a low charge transfer resistance (81.98 Ω) and hence low electron conductivity. For comparison, the pure IDT cathode has a higher charge transfer resistance (264.8 Ω). Also, the large slope in the low frequency band indicates the rapid ion diffusion. The findings evidence that the construction of IDT@IDT-1000 through π-π stacking greatly improves the reaction kinetics of the cathodes.

4. Conclusions

In summary, we proposed a strategy of extending molecular framework to inhibit the dissolution of electrode materials and enhance Li^+/e^{-1} transport ability. The stronger intermolecular interactions (π-π conjugation and H-bond) were the key reasons to increase the conductivity and stability of active cathodes. Specifically, the electrical conductivity of IDT-based material was increased by promoting the electron delocalization, and the IDT-based layered materials were also able to boost the ionic transport. Such a rational design endowed the IDT@IDT-1000 electrodes with a higher average coulomb efficiency (~99.0%), a higher reversible specific capacity (238 mAh g^{-1} as early discharge capacity and >200 mAh g^{-1} after 1000 cycles at 0.2C) and a markable rate performance (105 mAh g^{-1} at 5.0C). Moreover, the discharge voltage increased as a whole during cycling due to the homogenization and dilution of electron cloud density on conjugated surface of the active materials. The novel concept of extending the conjugate skeleton to balance the solubility and kinetic properties, produces worthful findings which may open new pathways for the development of advanced organic cathodes for LIBs.

CRediT authorship contribution statement

Liyi Zhao: Conceived and designed the research, Collected the . **Yunfei Ning:** Collected the . **Qingyu Dong:** Collected the . **Zaka Ullah:** Participated in discussions of the research. **Penghao Zhu:** Participated in discussions of the research. **Surong Zheng:** Participated in discussions of the research. **Guang Xia:** provided valuable discussions and modified the manuscript. **Shoupu Zhu:** provided valuable discussions and modified the manuscript. **Qi Li:** Conceived and designed the research, Wrote and modified the manuscript, Supervision. **Liwei Liu:** Supervision.

Declaration of competing interest

The authors declare that they have no known competing financial interests or personal relationships that could have appeared to influence the work reported in this paper.

Data availability

Data will be made available on request.

Acknowledgements

This work was supported by National Natural Science Foundation of China (Grant Nos. 51972330), the Military Commission Logistics Department (Grant Nos. BY117J013), the State Key Program of National Natural Science Foundation of China (Grant No. 61734008), the Natural Science Foundation of Jiangsu Province (Grant No. BK20210129) and Jiangsu Funding Program for Excellent Postdoctoral Talent. The authors are grateful to Platforms of Characterization & Test, Collaborative Innovation Center of Suzhou Nano Science and Technology, and Nanofabrication Facility from Suzhou Institute of Nano-Tech and Nano-Bionics, for their technical support of Nano-X and provision of experimental facilities.

Appendix A. Supplementary data

Supplementary data to this article can be found online at https://doi.org/10.1016/j.jpowsour.2022.232518.

References

[1] Z. Lin, H.Y. Shi, L. Lin, X. Yang, W. Wu, X. Sun, Nat. Commun. 12 (2021) 4424.
[2] F. Xu, H. Wang, J. Lin, X. Luo, S.-a. Cao, H. Yang, J. Mater. Chem. 4 (2016) 11491–11497.
[3] Y. Lu, X. Hou, L. Miao, L. Li, R. Shi, L. Liu, J. Chen, Angew Chem. Int. Ed. Engl. 58 (2019) 7020–7024.
[4] W. Ai, W. Zhou, Z. Du, C. Sun, J. Yang, Y. Chen, Z. Sun, S. Feng, J. Zhao, X. Dong, W. Huang, T. Yu, Adv. Funct. Mater. 27 (2017).
[5] J. Tong, C. Han, X. Hao, X. Qin, B. Li, ACS Appl. Mater. Interfaces 12 (2020) 39630–39638.
[6] S. Guerin, D. Thompson, Nat. Mater. 20 (2021) 574–575.
[7] Y. Zhen, C. Zhang, J. Yuan, Y. Li, J. Mater. Chem. 9 (2021) 22056–22063.
[8] N. Patil, A. Aqil, F. Ouhib, S. Admassie, O. Inganas, C. Jerome, C. Detrembleur, Adv. Mater. 29 (2017).
[9] T. Liu, K.C. Kim, B. Lee, S. Jin, M.J. Lee, M. Li, S. Noda, S.S. Jang, S.W. Lee, ACS Appl. Energy Mater. 3 (2020) 3728–3735.
[10] Y. Xu, B. Pan, W.S. Li, L. Dong, X. Wang, F.G. Zhao, ACS Appl. Mater. Interfaces 13 (2021) 41537–41544.
[11] Y. Chen, C. Wang, Acc. Chem. Res. 53 (2020) 2636–2647.
[12] M. Li, J. Yang, Y. Shi, Z. Chen, P. Bai, H. Su, P. Xiong, M. Cheng, J. Zhao, Y. Xu, Adv. Mater. 34 (2022), e2107226.
[13] Q. Pan, Y. Zheng, Z. Tong, L. Shi, Y. Tang, Angew Chem. Int. Ed. Engl. 60 (2021) 11835–11840.
[14] S. Bai, B. Kim, C. Kim, O. Tamwattana, H. Park, J. Kim, D. Lee, K. Kang, Nat. Nanotechnol. 16 (2021) 77–84.
[15] K. Xu, H. Sun, T.P. Ruoko, G. Wang, R. Kroon, N.B. Kolhe, Y. Puttisong, X. Liu, D. Fazzi, K. Shibata, C.Y. Yang, N. Sun, G. Persson, A.B. Yankovich, E. Olsson, H. Yoshida, W.M. Chen, M. Fahlman, M. Kemerink, S.A. Jenekhe, C. Muller, M. Berggren, S. Fabiano, Nat. Mater. 19 (2020) 738–744.
[16] Y. Morita, S. Nishida, T. Murata, M. Moriguchi, A. Ueda, M. Satoh, K. Arifuku, K. Sato, T. Takui, Nat. Mater. 10 (2011) 947–951.
[17] M. Yao, S.-i. Yamazaki, H. Senoh, T. Sakai, T. Kiyobayashi, Mater. Sci. Eng. B 177 (2012) 483–487.
[18] S. Xu, H. Li, Y. Chen, Y. Wu, C. Jiang, E. Wang, C. Wang, J. Mater. Chem. 8 (2020) 23851–23856.
[19] C. Wang, Y. Xu, Y. Fang, M. Zhou, L. Liang, S. Singh, H. Zhao, A. Schober, Y. Lei, J. Am. Chem. Soc. 137 (2015) 3124–3130.
[20] M. Tang, S. Zhu, Z. Liu, C. Jiang, Y. Wu, H. Li, B. Wang, E. Wang, J. Ma, C. Wang, Chem 4 (2018) 2600–2614.
[21] S. Xu, H. Dai, S. Zhu, Y. Wu, M. Sun, Y. Chen, K. Fan, C. Zhang, C. Wang, W. Hu, eScience 1 (2021) 60–68.
[22] Y. Shen, X. Shen, M. Yang, J. Qian, Y. Cao, H. Yang, Y. Luo, X. Ai, Adv. Funct. Mater. 31 (2021).
[23] Z. Song, Y. Qian, M. Otani, H. Zhou, Adv. Energy Mater. 6 (2016).
[24] B. Pan, L. Bai, C.M. Hu, X. Wang, W.S. Li, F.G. Zhao, Adv. Energy Mater. 10 (2020).
[25] Y. Chen, M. Tang, Y. Wu, X. Su, X. Li, S. Xu, S. Zhuo, J. Ma, D. Yuan, C. Wang, W. Hu, Angew Chem. Int. Ed. Engl. 58 (2019) 14731–14739.
[26] M. Kolek, F. Otteny, P. Schmidt, C. Mück-Lichtenfeld, C. Einholz, J. Becking, E. Schleicher, M. Winter, P. Bieker, B. Esser, Energy Environ. Sci. 10 (2017) 2334–2341.
[27] Y. Chen, H. Li, M. Tang, S. Zhuo, Y. Wu, E. Wang, S. Wang, C. Wang, W. Hu, J. Mater. Chem. 7 (2019) 20891–20898.
[28] J. Gu, Y. Gu, S. Yang, Chem. Commun. 53 (2017) 12642–12645.
[29] A. Suryawanshi, D. Mhamane, S. Nagane, S. Patil, V. Aravindan, S. Ogale, M. Srinivasan, Electrochim. Acta 146 (2014) 218–223.
[30] H. Zhang, Y. Fang, F. Yang, X. Liu, X. Lu, Energy Environ. Sci. 13 (2020) 2515–2523.
[31] B. Delley, J. Chem. Phys. 92 (1990) 508–517.
[32] S. Chen, J. Zheng, D. Mei, K.S. Han, M.H. Engelhard, W. Zhao, W. Xu, J. Liu, J. G. Zhang, Adv. Mater. 30 (2018), e1706102.
[33] M.J. Harrison, D.P. Woodruff, J. Robinson, Surf. Sci. 600 (2006) 1827–1836.
[34] S. Bu, N. Yao, M.A. Hunter, D.J. Searles, Q. Yuan, NPJ Comput. Mater. 6 (2020).
[35] J.H. Hou, M.Y. Yang, Q. Dou, Q. Chen, X.Z. Wang, C.G. Hu, R. Paul, Chem. Eng. J. 450 (2022), 138425.
[36] H.J. Monkhorst, J.D. Pack, Phys. Rev. B 13 (1976) 5188–5192.
[37] Z. Ye, S. Xie, Z. Cao, L. Wang, D. Xu, H. Zhang, J. Matz, P. Dong, H. Fang, J. Shen, M. Ye, Energy Storage Mater. 37 (2021) 378–386.